In-line particle holography with an astigmatic beam: set-up self-calibration using an "inverse problems" approach

Nicolas Verrier, Corinne Fournier, Loïc Méès, Thierry Fournel

In-line particle holography with an astigmatic beam: set-up self-calibration using an "inverse problems" approach

Nicolas Verrier,[1,*] Corinne Fournier,[1] Loic Méès,[2] and Thierry Fournel[1]

[1] *Université de Lyon, F-42023 Saint-Etienne, France,*
CNRS UMR 5516 Laboratoire Hubert Curien, F-42000 Saint-Etienne, France,
Université de Saint-Etienne Jean Monnet, F-42000 Saint-Etienne, France.
[2] *Laboratoire de Mécanique des Fluides et d'Acoustique (LMFA),*
UMR CNRS 5509 Ecole Centrale de Lyon, Centre National de la Recherche Scientifique,
Université Claude Bernard Lyon 1, INSA de Lyon,
36 avenue Guy de Collongue, F-69134 Ecully, France

compiled: August 26, 2014

The use of digital in-line holography for the characterization of confined flows in cylindrical geometry confinements (e.g. cylindrical pipe or cylindrical capillaries) is discussed. Due to cylindrical geometry of the walls, the illuminating laser wave can be strongly astigmatic, which renders the use of classical reconstruction techniques impossible. Contrary to plane wave holography set-up, the diffraction pattern of the particles strongly depends on the axial distance of the latter to the entry face of the confinement structure. To address this reconstruction issue, we propose to use an "inverse problems" approach. This approach amounts to finding the best match (least squares solution) between a diffraction pattern model and the captured hologram. For this purpose, a direct imaging model for astigmatic holograms, based on the use of transfer matrices is presented and validated by comparing experimental and simulated holograms. The accuracy of the "inverse problems" reconstruction is then used to calibrate the experimental set-up adjustable parameters. Finally, the approach is tested through experimental astigmatic hologram reconstruction, thus paving the way to its use in pipe flow studies.

OCIS codes: (090.1995) Holography: Digital holography, (100.3190) Image processing: Inverse problems, (100.3010) Image reconstruction techniques; (120.3940) Metrology

http://dx.doi.org/10.1364/XX.99.099999

1. Introduction

Originally proposed by Gabor as an improvement of electronic microscopy configuration [1, 2], digital in-line holography aims at recording, on a lensless digital sensor (first holograms were recorded on high resolution photographic plates) the interference between the wave disturbance due to objects (the object beam) and the part of the wave that does not interact with the objects (the reference beam). These captured holograms contain the whole amplitude and phase information of the optical field diffracted by the studied objects. Information extraction is classically realized by calculating the light back-propagation to the plane where the studied object is located [3–5]. Due to its intrinsic properties (e.g. 3D imaging, full optical field retrieval), digital holography has found interest in various studies such as fluid dynamics [6], mechanical inspection [7], or biomedical imaging [8]. However, as amplitude and phase information are recorded onto an intensity sensitive medium, they can not be easily separated and therefore, reconstructed holograms exhibit the so-called twin-image noise. Experimental elimination of the twin-image noise is made possible through the use of off-axis holography [9]. However, in this case most of the spatial frequency bandwidth of the sensor is lost (it is in fact occupied by the unwanted autocorrelation contribution and twin-image terms of the intensity

* nicolas.verrier@univ-st-etienne.fr

distribution).

To improve the accuracy of classical in-line holographic imaging, direct hologram signal processing was proposed, thus eliminating the light backpropagation calculation. Most of the suggested methods are based on the direct analysis of spatial frequency content of the recorded holograms. To this purpose, Menzel proposed a 1D analysis of intensity profiles for particle holograms [10], based on particle hologram models fitting [11]. Spatial frequency analysis through the use of Wigner transform has been also proposed but, it is limited to the characterization of 1D profiles. As a matter of fact, Wigner transformation of a 2D signal results in a 4D representation [12]. Digital filtering based on the use of a truncated inverse filter as also been demonstrated and proved to reconstruct hologram without twin-image disturbance [13].

In contrast to these optical approaches, signal processing tools, commonly used in the image processing of other imaging modalities, provide a rigorous way to extract on-axis hologram information leading to optimal image processing in certain cases. Rather than transforming the hologram, it aims at finding the reconstruction that best models the measured hologram [14, 15]. This "Inverse Problems" Approach (IPA) extracts more information from the hologram and is proved to solve two essential issues in digital holography: the improvement of the accuracy of the reconstruction [16], and the enlargement of the studied field beyond the physical limit of the sensor size [17]. It also leads to almost unsupervised algorithms (only few tuning parameters are used) [18]. These approaches are sometimes referred to as compressive sensing methods [19–22].

Implementing such approaches requires a precise knowledge of the hologram formation model. In the case of a non-confined flow containing spherical particles, the imaging model has been accurately described either for collimated or divergent reference beams [23, 24]. However, such models are not suited when dealing with cylindrical confinements such as pipes. As a matter of fact, the cylindrical structure of the pipe through which holograms are recorded introduces astigmatism that is not taken into account in classical models. However, astigmatism compensation in digital hologram reconstruction has been extensively studied, and successfully applied using modified chirped reconstruction kernels [25–27]. In-Situ compensation using index matching liquids have been also investigated [28]. Recently, an hologram formation model

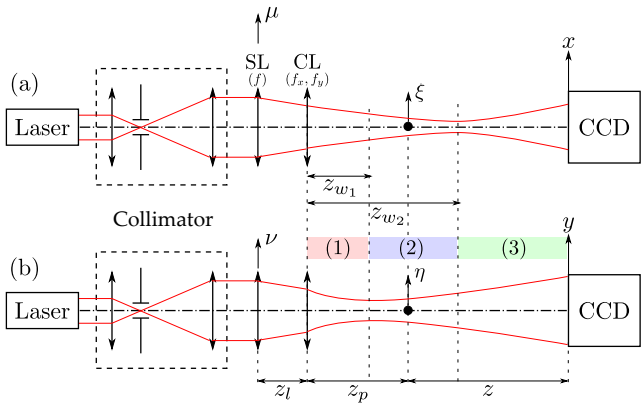

Fig. 1. (Color online) Experimental configuration for digital hologram recording with an astigmatic reference beam. (a) x, z view. (b) y, z view. SL: Spherical Lens, CL: Cylindrical Lens

that takes into account the astigmatism due to pipe-flows and micropipe-flows has been proposed and validated [29, 30]. This semi-analytic calculation approach is based on the use of transfer matrix systems. We suggest, in this paper, to use this direct model in order to achieve inverse reconstruction of digital holograms.

In this article, we propose to reconstruct digital holograms recorded with an astigmatic reference beam using IPA reconstruction. In the first part of the article, the general formalism of holographic recording with an astigmatic reference beam is described. Then, the IPA hologram reconstruction algorithm, based on the astigmatic imaging model, is presented. A self-calibration scheme, relying on the accuracy of the IPA algorithm and our set-up specificity is then proposed. Finally, the ability of this approach to deal with astigmatic hologram is demonstrated through the analysis of experimental holograms, thus illustrating its applicability to confined flow studies.

2. Digital in-line holography with an astigmatic reference beam: experimental configuration

In order to model the effect of a confinement structure on the imaging system, the experimental configuration proposed in Fig. 1 is considered. It consists of an in-line digital holographic set-up, where astigmatism is brought and controlled by a spherical/cylindrical lens doublet. The light emitted by a $\lambda = 635$ nm, 80 mW laser diode (Z-Laser®) is filtered and collimated. The generated "plane-wave" is then focalized using a spherical lens (SL) with focal length $f = 125$ mm. A cylindrical lens (CL, $f_x \to \infty$, $f_y = 200$ mm), positioned at a distance z_l

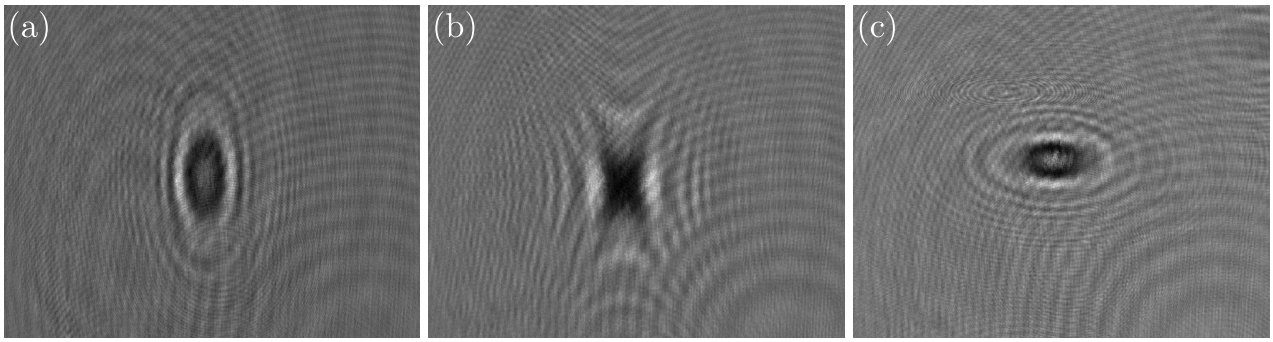

Fig. 2. Experimental acquisition of a 100 μm in diameter particle for (a) $z_p \approx 55$ mm, $z \approx 165$ mm ; (b) $z_p \approx 80$ mm, $z \approx 140$ mm ; $z_p \approx 120$ mm, $z \approx 100$ mm. Experimental parameters are roughly estimated by direct measurements on the set-up.

from SL is used to generate astigmatism. A control of the amount of astigmatism is possible by acting on z_l. Due to the astigmatism, the reference beam exhibits two waists in both horizontal and vertical directions. The studied object is located at a distance z_p from CL. Interference between the wave diffracted by the object and the reference wave is finally recorded on a CCD sensor positioned at a distance z from the object.

Depending on the particle position compared to the beam waist positions, the recorded interference pattern exhibits different shapes [31]: particles located in areas (1) and (3) lead to elliptical fringe patterns, whereas particles in region (2) are characterized by the hyperbolic shape of their interference patterns. The different patterns are illustrated by Fig. 2. Experimental holograms are recorded with a distance from CL to the CCD sensor sets to $z_p + z \approx 220$ mm. The considered object is an opaque chromium disk of diameter 100 μm $\pm$ 1 μm (roundness $\pm$ 0.25 μm) deposited on a glass slide (Optimask®). Holograms are acquired on a 1280×1024 square pixel 12-bits CCD camera with 6.7 μm pitch (PCO Intellicam®). The distance between both lenses is fixed to $z_l \approx 17$ mm. Within this configuration, the two beam waists are respectively positioned at $z_{w_1} \approx 70$ mm and at $z_{w_2} \approx 110$ mm. Therefore the three areas illustrated in Fig. 1 extend from $z_p = 0$ mm to $z_p \approx 70$ mm for zone (1), from $z_p \approx 70$ mm to $z_p \approx 110$ mm for the second area, and finally from $z_p \approx 110$ mm to $z_p \approx 220$ mm for the last region. Recorded holograms are shown in Fig. 2 with: $z_p \approx 55$ mm, $z \approx 165$ mm (Fig. 2(a)), $z_p \approx 80$ mm, $z \approx 140$ mm (Fig. 2(b)), and $z_p \approx 120$ mm, $z \approx 100$ mm (Fig. 2(c)). Here one can realize that the expected behaviors, predicted in Ref. [31] are found.

In this article, we apply an IPA to process holograms recorded under astigmatic conditions. To successfully apply this approach, an accurate imaging model is needed. For this purpose, in the next section, the model of particle holograms under astigmatic beam illumination is presented.

3. Direct model of hologram formation using an astigmatic reference beam

The image formation model for the experimental test set-up (Fig. 1) takes into account the reference wave astigmatism due to both SL and CL. The optical configuration is considered as a linear system. Under paraxial conditions, the image formation can be modeled using transfer matrix system [29, 32, 33].

Propagation of the light through the optical system is divided into two distinct linear systems. The first one considers light propagation from SL to the particle taking into account the effect of both SL and CL. The second system models the light propagation and the diffraction from the object plane to the CCD sensor plane. Such propagation is modeled by a generalization of the Fresnel transformation to the so called ABCD systems [34].

Thus, calculation of light propagation from the SL (coordinate system (μ, ν)) to the particle plane (coordinate system (ξ, η) see Fig. 1 for details) is performed considering

$$\begin{aligned}\mathcal{G}_1(\xi,\eta) = \frac{\exp\left(i\frac{2\pi}{\lambda}\sqrt{B_1^x B_1^y}\right)}{i\lambda\sqrt{B_1^x B_1^y}} \int_{\mathbb{R}^2} \mathcal{G}(\mu,\nu) \\ \times \exp\left[i\frac{\pi}{\lambda B_1^x}\left(A_1^x\mu^2 - 2\xi\mu + D_1^x\xi^2\right)\right] \\ \times \exp\left[i\frac{\pi}{\lambda B_1^y}\left(A_1^y\nu^2 - 2\eta\nu + D_1^y\eta^2\right)\right] d\mu d\nu, \quad (1)\end{aligned}$$

where $A_1^{x,y}$, $B_1^{x,y}$, and $D_1^{x,y}$ are the transfer matrix

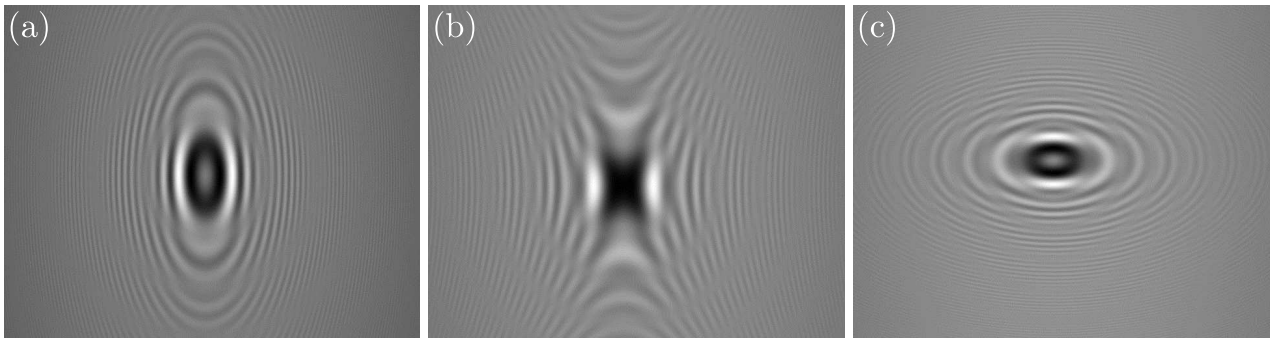

Fig. 3. Simulation of a 100 μm in diameter particle hologram corresponding to experimental data of Fig. 2. Discussion about accurate parameter estimation is proposed in Sections 5 and 6.

coefficients for the first transfer system (defined in Appendix A, Eq. (18)). The collimated Gaussian radiation $\mathcal{G}(\mu,\nu)$ impinging SL is here given by

$$\mathcal{G}(\mu,\nu) = \exp\left(-\frac{\mu^2+\nu^2}{\omega_0^2}\right). \tag{2}$$

Here, ω_0 is the $1/e$ beam radius. After mathematical developments Eq. (1) can be written

$$\mathcal{G}_1(\xi,\eta) = \frac{\exp\left(i\frac{2\pi}{\lambda}\sqrt{B_1^x B_1^y}\right)}{i\lambda\sqrt{B_1^x B_1^y}} K_1^x K_1^y \exp\left[-\left(\frac{\xi^2}{\omega_\xi^2}+\frac{\eta^2}{\omega_\eta^2}\right)\right] \exp\left[-i\frac{\pi}{\lambda}\left(\frac{\xi^2}{R_\xi}+\frac{\eta^2}{R_\eta}\right)\right], \tag{3}$$

where the complex amplitude factors $K_1^{x,y}$, the beam waists $\omega_{\xi,\eta}$, and the wavefront curvature $R_{\xi,\eta}$ after propagation through the first transfer system are defined in Appendix B.

Within the same formalism, one can derive the amplitude in the sensor plane after propagation through the second transfer system

$$\mathcal{G}_2(x,y) = \frac{\exp\left(i\frac{2\pi}{\lambda}\sqrt{B_2^x B_2^y}\right)}{i\lambda\sqrt{B_2^x B_2^y}} \int_{\mathbb{R}^2} \mathcal{G}_1(\xi,\eta) \times [1-T(\xi,\eta)] \exp\left[i\frac{\pi}{\lambda B_2^x}\left(A_2^x\xi^2 - 2x\xi + D_2^x x^2\right)\right] \times \exp\left[i\frac{\pi}{\lambda B_2^y}\left(A_2^y\eta^2 - 2y\eta + D_2^y y^2\right)\right] d\xi d\eta, \tag{4}$$

where $A_2^{x,y}$, $B_2^{x,y}$, and $D_2^{x,y}$ are the transfer matrix coefficients for the second transfer system (defined in Appendix A, Eq. (19)).

The transmittance function of the object, denoted $1-T(\xi,\eta)$, can be decomposed on a Gaussian function basis so that Eq. (4) can be analytically derived [35]. It can be written as

$$T(\xi,\eta) = \sum_{k=1}^{N} A_k \exp\left[-\frac{B_k}{r^2}\left(\xi^2+\eta^2\right)\right], \tag{5}$$

with r being the simulated particle/aperture radius (elliptical objects can also be considered within this framework). Coefficients A_k and B_k are determined through iterative calculation of the Kirchhoff propagation equation of a hard edge [35]. Their values, which are complex, depend on the amount of basis functions considered for Kirchhoff equation resolution. From Eq. (4) it is possible to derive analytical expressions of both reference $\mathcal{R}(x,y)$ and object $\mathcal{O}(x,y)$ fields so that

$$\mathcal{G}_2(x,y) = \frac{\exp\left(i\frac{2\pi}{\lambda}\sqrt{B_2^x B_2^y}\right)}{i\lambda\sqrt{B_2^x B_2^y}} \left[\mathcal{R}(x,y) + \mathcal{O}(x,y)\right]. \tag{6}$$

The reference and the object fields can therefore be obtained as

$$\mathcal{R}(x,y) = \frac{\exp\left(i\frac{2\pi}{\lambda}\sqrt{B_1^x B_1^y}\right)}{i\lambda\sqrt{B_1^x B_1^y}} K_1^x K_1^y K_2^x K_2^y \times \exp\left[-\frac{\pi}{\lambda}\left(\frac{N_x}{B_2^x}x^2 + \frac{N_y}{B_2^y}y^2\right)\right] \times \exp\left[i\frac{\pi}{\lambda}\left(\frac{M_x}{B_2^x}x^2 + \frac{M_y}{B_2^y}y^2\right)\right], \tag{7}$$

and

$$\mathcal{O}(x,y) = \frac{\exp\left(i\frac{2\pi}{\lambda}\sqrt{B_1^x B_1^y}\right)}{i\lambda\sqrt{B_1^x B_1^y}} K_1^x K_1^y \times \exp\left[i\frac{\pi}{\lambda}\left(\frac{D_2^x}{B_2^x}x^2 + \frac{D_2^y}{B_2^y}y^2\right)\right] \sum_{k=1}^{N} A_k K_2^{x_{eq}} K_2^{y_{eq}} \times \exp\left[-\frac{\pi}{\lambda}\left(\frac{N_{x_{eq}}}{B_2^x}x^2 + \frac{N_{y_{eq}}}{B_2^y}y^2\right)\right] \times \exp\left[i\frac{\pi}{\lambda}\left(\frac{M_{x_{eq}}}{B_2^x}x^2 + \frac{M_{y_{eq}}}{B_2^y}y^2\right)\right]. \quad (8)$$

The values of the different parameters of Eqs. (7) and (8) can be found in Appendix B.

Thus, it is possible to simulate the recorded intensity distribution $g(x,y)$ considering

$$g(x,y) = \mathcal{G}_2(x,y)\,\mathcal{G}_2^*(x,y). \quad (9)$$

It should be noted that the position of the transvere interference pattern in the sensor plane (x_0, y_0), can be easily linked to the transverse position of the object (ξ_0, η_0) considering classical geometrical optics relationships

$$\xi_0 = \frac{|z_p - z_{w_2}| \pm z}{|z_p - z_{w_2}|} x_0, \;\; \eta_0 = \frac{|z_p - z_{w_1}| \pm z}{|z_p - z_{w_1}|} y_0 \quad (10)$$

where the $\pm$ sign depends on the location of the object compared to each waist. It is positive if the object is located after the considered waist and negative otherwise.

To illustrate the ability of the proposed model to simulate the experimental holograms acquired with our set-up (Fig. 1), the intensity distributions are computed using parameters close to the roughly estimated experimental parameters of the holograms shown in Fig. 2. The simulations are proposed in Fig. 3. Here, a qualitative agreement between the model and the data is noticeable (a more quantitative discussion is proposed Sec. 6). Thus, this model can be considered for the use of IPA for astigmatic hologram processing.

In the following section we use it as a direct model in our IPA reconstruction procedure.

4. Hologram reconstruction through "inverse problems" approach

Depending on the type of object under study two different IPA can be considered. For simple shaped objects (described by few parameters), with diffraction pattern models given by an analytical formula, a model-fitting approach [14] or a greedy approach [16, 36] can be used. More complex objects (*i.e.* non parametric objects) can be described by an opacity distribution sampled on a 3-D grid. The amplitude of the opacity distribution can be estimated by inverting the hologram formation model, using a suitable regularization as typically done when dealing with ill-conditioned inverse problems [37].

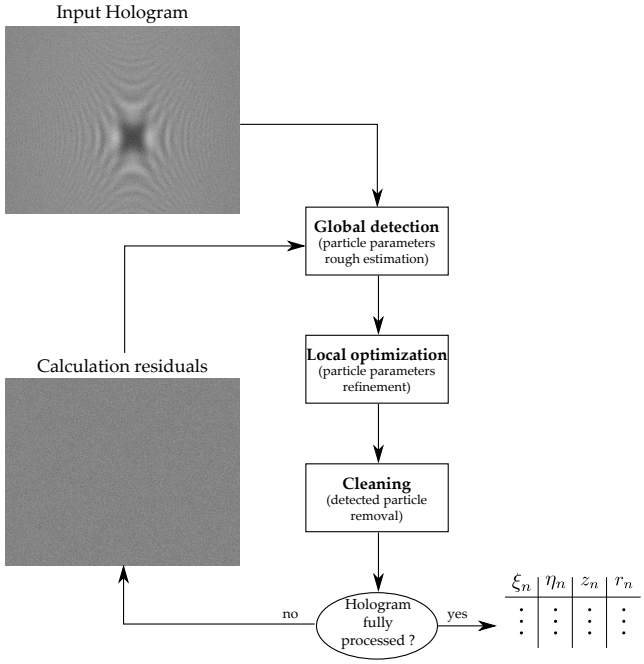

Fig. 4. Synoptics of the "inverse problems" approach algorithm.

In this article, only simple shaped objects (particles, bubbles or droplets) are considered, and the greedy algorithm first proposed by Soulez *et al.* [16, 17] is used. It solves the reconstruction problem iteratively. The objects are successively detected, aiming in each iteration at finding the best fit (least squares solution) between the model and the experimental hologram. It consists of three steps, summarized on Fig. 4:

- a global detection step (or a coarse estimation step), which finds the best-matching element in a discrete dictionary of direct models (*i.e.* a model for each 3-D location and shape),
- a local optimization step (or a refinement step), which fits the selected diffraction pattern to the data for sub-pixel estimation,
- a cleaning step, which subtracts the detected pattern from the hologram to increase the signal-to-noise ratio of the remaining objects and suppress Moiré effect.

The procedure is then repeated on the residuals until no more object is detected.

Assuming the lens focal distances given by manufacturer specifications, unknown optical set-up parameters are reduced to (z_l, $z_{\text{tot}} = z_p + z$). Using IPA, accurate estimation of the object parameters (x_n, y_n, z_n, r_n) and optical set-up parameters can be obtained for each hologram. However, as far as the experimental configuration parameters are fixed, we propose, in the following section, to take benefits of both the accuracy of the inverse approach and of the set-up singularities to accurately calibrate z_l and z_{tot} only once, therefore resulting in a faster particle parameter estimation.

5. Self-calibration of the experimental configuration using "inverse problems" approach

We propose to take benefits of the IPA reconstruction recalled in Sec. 4, to achieve accurate self calibration of our experimental configuration. In this step, two key parameters are to be accurately assessed: z_l and $z_{\text{tot}} = z_p + z$. These parameter estimations can be performed with a calibrated object (as the one used in Section 2) at any distance from the sensor. However due to the singularities of the set-up, some z_p ranges are more suitable for accurate estimations. In this Section, we first study the Cramèr-Rao Lower Bounds (CRLB) on the standard deviation of z_l and z, then we detail the implementation of the self-calibration step.

5.A. Accuracy of the estimation of set-up parameters

In estimation theory [38], lower bounds on the variance of any unbiased estimator of a model parameter can be evaluated using CRLB computations [39, 40]. It consists in computing the inverse of Fisher information matrix. In the case of white Gaussian noise, each element of this matrix is proportional to the numerical integration of the image formation model gradients in the direction of the model's parameters and to the Signal to Noise Ratio of the hologram (see [39] for more details). These theoretical bounds are reached asymptotically (for large data) by the maximum likelihood estimator. CRLB on z_l and z parameters are computed using the direct model given in Section 3 with experimental parameters given in Section 2. Their evolution versus z_p position is shown in Fig. 5.

The plot of the CRLB on parameter z_l (Fig. 5(a)) shows two main minima at waist positions (dashed line on Fig. 5) and one secondary minimum in-between the two waists. The main minima are due to the high values of the gradient of the model versus z (Fig. 5(b)) on the waist locations. The secondary minimum position corresponds to a change in the hyperbolic diffraction pattern which becomes an equilateral hyperbola (*i.e.* hyperbola asymptotes are perpendicular) at this position. On one hand, the best accuracy of z and z_l is achieved in the waist planes. On the other hand, the illumination field is narrow in the focalization direction (about 1 μm for both waists) and "large" in the other direction (from 6 mm to 9 mm). Thus, they cannot be used for imaging purposes, but these singularities can be taken advantage of for calibration step. In the next section, a calibration scheme is proposed.

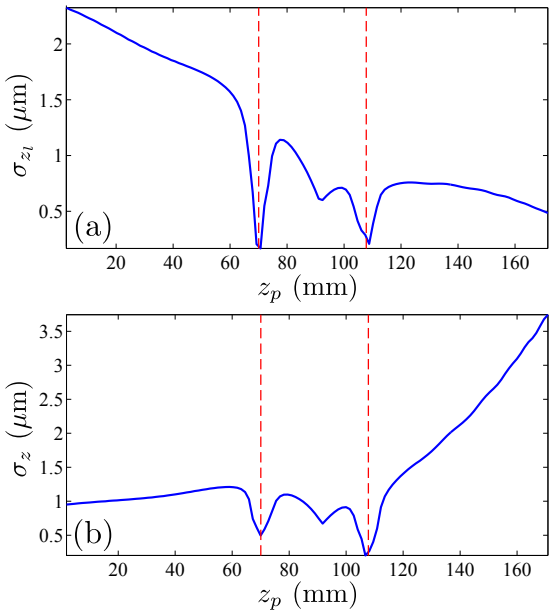

Fig. 5. (Color Online) Theoretical study of the evolution of (a) σ_{z_l} and (b) σ_z standard deviations versus the distance z_p between CL and the object. The experimental parameters are the same as in Section 2. Red dashed lines are associated with beam waist positions.

5.B. Self-calibration of the set-up

The distance z_l between the lenses, and the distance z_{tot} between the CL and the sensor are strongly correlated: any error on one parameter estimation is propagated to the other one, preventing from their simultaneous optimization. Therefore, we consider their optimization according to two successive steps. The first step consists in optimizing the z_l distance (z_{tot} being fixed) to obtain both waist positions compared to CL: z_{w_1} and z_{w_2}. The second step, is the estimation of z_{tot} considering the z_l value of the earlier step. As waist positions are fixed by the first step, it consists in estimating the

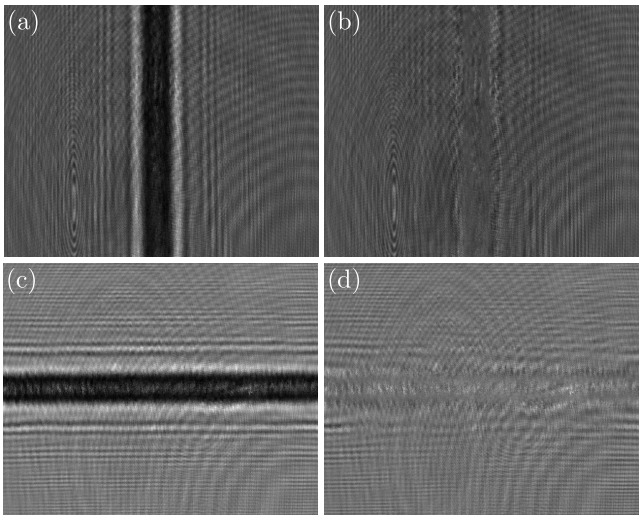

Fig. 6. Calibration of z_l. (a) Hologram recorded with a $2r = 100\mu$m object centered in the first beam waist (z_{w_1} from CL), z_{tot} is fixed to 220 mm. (b) Calculation residuals after IPA reconstruction procedure. (c) Hologram recorded with a $2r = 100\mu$m object centered in the second beam waist ($z_{\text{tot}} - z_{w_2}$ from CCD). (d) Calculation of the residuals after IPA reconstruction procedure. Here, z_l is fixed to the value obtained according to the optimization values obtained for the hologram (a).

distance between the second beam waist and the sensor.

The experimental self-calibration of the two parameters z_{tot} and z_l is illustrated on Fig. 6. An opaque chromium disk ($2r = 100\mu$m in diameter) is positioned in the center of the first beam waist located at z_{w_1} from CL. A precise experimental positioning of the object in the waists is possible due to the singular shape of the recorded holograms. As the first waist is horizontal, the recorded interference pattern exhibits a vertical fringe shape (see Fig. 6(a)). For this calibration step, the distance between CL and the sensor is fixed to $z_{\text{tot}} = 220$ mm $\pm$ 1 mm. The reconstruction of the hologram shown on Fig. 6(a) is realized considering the algorithm depicted in the previous section with an estimation of the z_l parameter. The hologram model (presented in Sec. 3), is then subtracted to the original hologram leading to the calculation of the residuals presented on Fig. 6(b). Best estimated parameters are $\xi_0 = 44.02$ μm, $\eta_0 = -1.12$ μm, $z = 148.9$ mm, $r = 47.4$ μm, and $z_l = 17.2$ mm. Value of ξ_0 is given with respect to the center of the field in the (ξ, η) plane. In this particular region, the waist width in η direction is about 1 μm. Thus, our circular particle is illuminated over a chord (instead of being illuminated over its whole area) resulting in a correlation between the estimate of the diameter and the estimate of the shift η_0. Therefore, the estimate of (r, η_0) is irrelevant. This point is confirmed by the underestimation of r. Nevertheless, these values are not used for this calibration step and only the obtained z_l value is kept for the further calibration of the z_{tot} distance.

For calibration of z_{tot}, our test object is positioned in the second beam waist. As a matter of fact, as both beam waist positions $z_{w_1} = 70.04$ mm, and $z_{w_2} = 107.80$ mm are determined by the z_l value, distance between the second waist and the sensor can be used to calibrate the sensor to CL distance. Therefore IPA reconstruction leads, in this case, to an accurate estimate of the particle to sensor distance z, with $z = z_{\text{tot}} - z_{w_2}$. The reconstruction is considered with an optimization of the z distance. Hologram obtained within this configuration is illustrated Fig. 6(c). Due to the fact that the particle is positioned in the second beam waist of Fig. 1, its interference pattern exhibits horizontal fringes. Calculation of the residuals after hologram reconstruction are depicted in Fig. 6(d). Best estimated parameters are $\xi_0 = -4.56$ μm, $\eta_0 = -6.40$ μm, $z = z_{\text{tot}} - z_{w_2} = 113.4$ mm, and $r = 48.9$ μm. As z_{w_2} is known, z_{tot} is found to be $z_{\text{tot}} = 221.2$ mm. As it was the case for the first calibration step, the value of r is under-estimated. However, as only information about z_{tot} is relevant for this part of the study, this diameter value does not affect the obtained results. Thus, in the remainder of this paper, the distance between both lenses z_l is fixed to $z_l = 17.2$ mm, and the distance between CL and the sensor will be $z_{\text{tot}} = 221.2$ mm.

By taking benefits of the astigmatic digital holographic configuration and using IPA reconstruction, we have been able to perform our experimental set-up calibration using two holograms recorded at singular positions: in the first beam waist, and in the second beam waist. The set-up being calibrated, we will be able to reconstruct experimental holograms by only considering the estimation of ξ_0, η_0, z, and r. In the final part of this article, experimental holograms of a calibrated pattern located in between the two waists are reconstructed using IPA with an astigmatic reference beam imaging model. The accuracy of such a reconstruction is evaluated.

6. "Inverse problems" approach reconstruction of experimental holograms

In this section, the reconstruction of holograms presented on Fig. 2 using IPA are considered. The

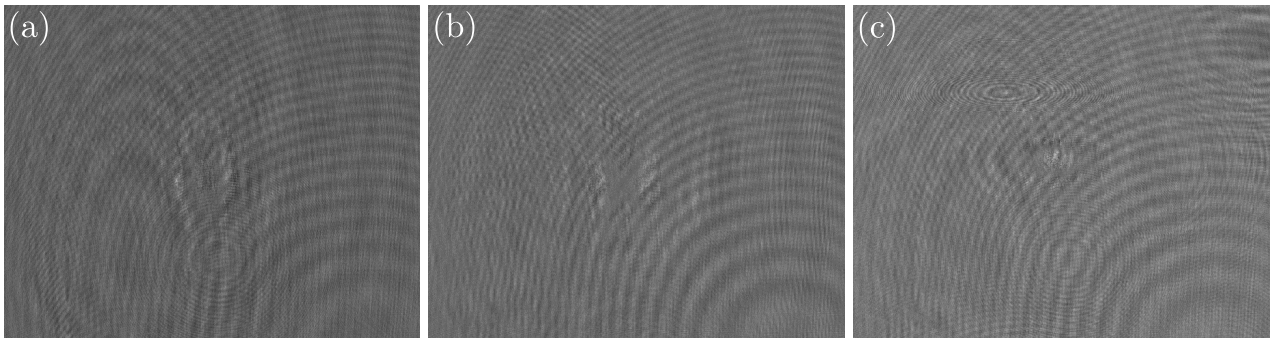

Fig. 7. Calculation residuals after "inverse problems" approach reconstruction of holograms proposed Fig. 2.

experimental calibration (Sec. 5) gives accurate values of z_l and z_{tot} that are used in the direct model computation. Therefore the global detection and local optimization steps, are performed only for ξ_0, η_0, z, and r. In order to assess the validity of our approach, the cleaned hologram are shown Fig. 7. It can be noticed that most of the interference pattern is efficiently removed (*i.e.* that the investigated object diffraction pattern is accurately estimated). However a part of the pattern remains visible. This might be linked to the fact that the considered imaging model relies on the paraxial approximation. Improvement of the particle detection is expected using a non paraxial imaging model [41, 42]. Nevertheless, the results presented on Tab. 1, show that reconstructed parameters are relevant: the particle radii estimate is in the range of the manufacturer specifications, and the z position estimate is coherent with rough measurements performed on the set-up. For a quantitative characterization of our reconstruction results, the normalized correlation coefficient, α_{norm}, between the acquired hologram d and the model g is computed. The closer α_{norm} to unity, the better the agreement between data and model. This coefficient is defined as

$$\alpha_{\text{norm}} = \sqrt{\frac{\sum_{i=1}^{N_{\text{pix}}} \bar{g}^2(i)}{\sum_{i=1}^{N_{\text{pix}}} \bar{d}^2(i)}}\ \alpha, \tag{11}$$

where $\bar{g}$ and $\bar{d}$ stand for zero-mean variables ($\bar{g}(i) = g(i) - N_{\text{pix}}^{-1} \sum_{i=1}^{N_{\text{pix}}} g(i)$), N_{pix} is number of pixels, and α is the scaling parameter between data and the model given by

$$\alpha = \frac{\sum_{i=1}^{N_{\text{pix}}} \bar{g}(i)\bar{d}(i)}{\sum_{i=1}^{N_{\text{pix}}} \bar{g}^2(i)}. \tag{12}$$

Calculated α_{norm} values are presented in the last column of Tab. 1. They are within the 0.6 to 0.8 interval, with an optimal value in region (2) that corresponds to a position close to the secondary minimum of Fig. 5(b). These α_{norm} values therefore reveals the qualitative agreement between experimental holograms and our imaging model. It should be noted that this area presents a large illuminating beam width and a good parameter estimation accuracy. Thus, it is suited for accurate quantitative imaging.

Table 1. Estimated particle parameters for each hologram. ξ_0 and η_0 positions are given, in the object plane, with respect to the optical axis.

Region	ξ_0 (μm)	η_0 (μm)	z (mm)	r (μm)	α_{norm}
(1)	65.0	-81.3	165.5	49.45	0.67
(2)	62.9	22.5	138.4	49.87	0.79
(3)	-18.7	-76.3	100.8	49.94	0.59

In order to evaluate the accuracy of the inverse approach reconstruction coupled with self calibration of the set-up, a statistical estimation of the error is performed. A data set of one hundred holograms is recorded with known lateral ($\Delta x, y =$ 20 μm) and axial ($\Delta z = 1$ mm) shifts of a calibrated object (the opaque disk of diameter $2r =$ 100 μm used in the previous experiments). The holograms are recorded within region (2) (see Fig. 1), that benefits from a large illumination area coupled with good axial parameters accuracy as illustrated in Fig. 5. Using the recorded data set the reconstructed opaque disk radius is estimated to be $r = 50.2$ μm with a standard deviation of 0.12 μm, which is in agreement with the manufacturer specifications. To calculate the accuracy of both axial and lateral measurements, each measurement is used to compute the distances between the estimated axial/lateral shifts and a fitted curve [43].

The standard deviation of these distances gives a rough estimation of the reconstruction accuracy of the axial and lateral shift.

Retrieved axial and lateral shifts are $\Delta z = 0.99$ mm, and $\Delta x, y = 19.9$ μm with a standard deviation of 0.03 mm, and 1.69 μm respectively. It should be noted that the estimated standard deviation on lateral shift values is higher than that of the other estimated parameters. This is due to the fact that paraxial approximation is no longer valid for the higher shift values, leading to a biased value of the standard deviation. More accurate estimate of this parameter is expected by considering a non-paraxial imaging model [41, 42]. Nevertheless, the proposed transfer matrix based imaging model can be considered as a valid direct model for hologram IPA reconstruction, thus paving the way for application in confined configurations such as pipe flows studies.

7. Conclusion

In this article we have discussed the use of IPA based on direct model parameter estimation for astigmatic digital hologram reconstruction. This IPA allows us to accurately estimate the set-up and the object parameters. However, the more the parameters to estimate, the longer the process. We have suggested using IPA reconstruction to first estimate accurately the experimental set-up parameters and then use them to accurately reconstruct particles. An image formation model based on transfer matrix modeling of optical components has been considered. It has been shown that the theoretical accuracy of the reconstruction is better in the beam waist area. Therefore, the set-up parameters have been estimated using two holograms of a calibrated pattern located in the beam waists. Using these parameters, we have then demonstrated that the IPA reconstruction of experimental holograms is successful and accurate for object located between the two waists. The accuracy on the object parameter reconstruction has been estimated through a statistical analysis of experimental holograms. Due to the shift-invariance of the used direct model, this reconstruction approach is limited to objects located in areas for which the paraxial approximation is satisfied. This limitation can be overcome using a more accurate model accounting for transverse shift-variance. Nevertheless, accurate particle parameter estimation has been successfully realized, thus illustrating the ability of our reconstruction scheme to further deal with confined flow hologram reconstruction.

Acknowledgments

This work was funded by the MORIN project (3D Optical Measurements for Research and INdustry), which is supported by the french government through the "Agence Nationale de la Recherche" (ANR) and the "Programme Avenir Lyon-Saint-Etienne" (PAL-SE). The Authors wishes to acknowledge Anthony Cazier for technical assistance.

Appendix A: Transfer matrix systems

Under paraxial conditions, each part of the experimental configuration proposed Fig. 1 can be expressed by independent transfer matrices.

Starting from $\mathcal{G}(\mu, \nu)$ defined Eq. (2), the beam first encounter SL, whose transfer matrix is [4]

$$M_{\mathrm{SL}} = \begin{pmatrix} 1 & 0 \\ -\frac{1}{f} & 1 \end{pmatrix}. \tag{13}$$

Then, the beam propagates over z_l

$$M_{z_l} = \begin{pmatrix} 1 & z_l \\ 0 & 1 \end{pmatrix}, \tag{14}$$

and is focalized by SL

$$M^x_{\mathrm{CL}} = \begin{pmatrix} 1 & 0 \\ -\frac{1}{f_x} & 1 \end{pmatrix}, \quad M^y_{\mathrm{CL}} = \begin{pmatrix} 1 & 0 \\ -\frac{1}{f_y} & 1 \end{pmatrix}. \tag{15}$$

Finally, after propagating over z_p to the particle plane

$$M_{z_p} = \begin{pmatrix} 1 & z_p \\ 0 & 1 \end{pmatrix}, \tag{16}$$

light impinges the sensor positioned at z from the particle

$$M_z = \begin{pmatrix} 1 & z \\ 0 & 1 \end{pmatrix}. \tag{17}$$

One can therefore define two transfer systems respectively governing light propagation before the object

$$M_1^{x,y} = M_{z_p} M_{\mathrm{CL}}^{x,y} M_{z_l} M_{\mathrm{SL}} = \begin{pmatrix} A_1^{x,y} & B_1^{x,y} \\ C_1^{x,y} & D_1^{x,y} \end{pmatrix}, \tag{18}$$

and light propagation/diffraction after the object

$$M_2^{x,y} = M_z = \begin{pmatrix} A_2^{x,y} & B_2^{x,y} \\ C_2^{x,y} & D_2^{x,y} \end{pmatrix}. \tag{19}$$

Appendix B: Beam waists and curvatures after propagation through transfer systems

1. Propagation in the first transfer system

The complex amplitude $\mathcal{G}_1(\xi,\eta)$ after propagation through the first transfer system to the particle plane is given by Eq. (3). Complex amplitude factors of this astigmatic Gaussian beam can be explicitly derived as

$$K_1^{x,y} = \left(\frac{\pi\omega_0^2}{1 - iA_1^{x,y}\frac{\pi\omega_0^2}{\lambda B_1^{x,y}}} \right)^{1/2}. \quad (20)$$

Beam waists and wavefront curvature radii are respectively given by

$$\omega_{\xi,\eta} = \left(\frac{\lambda B_1^{x,y}}{\pi\omega_0}\right)\left[1 + \left(A_1^{x,y}\frac{\pi\omega_0^2}{\lambda B_1^{x,y}}\right)^2\right]^{1/2}, \quad (21)$$

and

$$R(\xi,\eta) = -B_1^{x,y} \Bigg/ \left(D_1^{x,y} - \frac{A_1^{x,y}\left(\frac{\pi\omega_0^2}{\lambda B_1^{x,y}}\right)^2}{1 + \left(A_1^{x,y}\frac{\pi\omega_0^2}{\lambda B_1^{x,y}}\right)^2} \right). \quad (22)$$

2. Propagation in the second transfer system: reference field $\mathcal{R}(x,y)$

Complex amplitude factors $K_2^{x,y}$ in the sensor plane are given by

$$K_2^{x,y} = \left[\frac{\pi\omega_{\xi,\eta}^2}{1 + i\frac{\pi\omega_{\xi,\eta}^2}{\lambda B_2^{x,y}}\left(\frac{B_2^{x,y}}{R_{\xi,\eta}} - A_2^{x,y}\right)} \right]^{1/2}. \quad (23)$$

The values of $M_{x,y}$ and $N_{x,y}$ of Eq. (7) both give an insight of the beam waists and curvature and can be defined as

$$M_{x,y} = D_2^{x,y} + \frac{\left(\frac{\pi\omega_{\xi,\eta}^2}{\lambda B_2^{x,y}}\right)^2\left(\frac{B_2^{x,y}}{R_{\xi,\eta}} - A_2^{x,y}\right)}{1 + \left(\frac{\pi\omega_{\xi,\eta}^2}{\lambda B_2^{x,y}}\right)^2\left(\frac{B_2^{x,y}}{R_{\xi,\eta}} - A_2^{x,y}\right)^2}, \quad (24)$$

and

$$N_{x,y} = \frac{\left(\frac{\pi\omega_{\xi,\eta}^2}{\lambda B_2^{x,y}}\right)}{1 + \left(\frac{\pi\omega_{\xi,\eta}^2}{\lambda B_2^{x,y}}\right)^2\left(\frac{B_2^{x,y}}{R_{\xi,\eta}} - A_2^{x,y}\right)^2}. \quad (25)$$

3. Propagation in the second transfer system: object field $\mathcal{O}(x,y)$

Analytical expressions of $K_2^{x_{eq},y_{eq}}$, $M_{x_{eq},y_{eq}}$, and $N_{x_{eq},y_{eq}}$ can be derived from Eqs. (23), (24), and (25) by considering

$$\frac{1}{\omega_{\xi_{eq},\eta_{eq}}^2} = \frac{1}{\omega_{\xi,\eta}^2} + \frac{\Re\{B_k\}}{r^2}, \quad \frac{1}{R_{\xi_{eq},\eta_{eq}}} = \frac{1}{R_{\xi,\eta}} + \frac{\lambda\Im\{B_k\}}{\pi r^2}, \quad (26)$$

where $\Re\{.\}$, and $\Im\{.\}$ respectively denote real and imaginary parts of a complex number. Substituting $R_{\xi,\eta} \to R_{\xi_{eq},\eta_{eq}}$ and $\omega_{\xi,\eta} \to \omega_{\xi_{eq},\eta_{eq}}$ in Eqs. (23), (24), and (25), leads to analytical expressions of parameters $K_2^{x_{eq},y_{eq}}$, $M_{x_{eq},y_{eq}}$, and $N_{x_{eq},y_{eq}}$.

References

[1] D. Gabor, "A new microscopic principle," Nature **161**, 777–778 (1948).

[2] D. Gabor, "Microscopy by reconstructed wavefronts," Proc. R. Soc. Lon. Ser. A **197**, 454–487 (1949).

[3] U. Schnars and W. Jüptner, "Digital recording and numerical reconstruction of holograms," Meas. Sci. Technol. **13**, R85–R101 (2002).

[4] J. W. Goodman, *Introduction to Fourier optics* (Roberts and Company Publishers, 2005).

[5] N. Verrier and M. Atlan, "Off-axis digital hologram reconstruction: some practical considerations," Appl. Opt. **50**, H136–H146 (2011).

[6] J. Marié, N. Grosjean, L. Méès, M. Seifi, C. Fournier, B. Barbier, and M. Lance, "Lagrangian measurements of the fast evaporation of falling diethyl ether droplets using in-line digital holography and a high-speed camera," Exp. Fluids **55**, 1–13 (2014).

[7] M. Leclercq, M. Karray, V. Isnard, F. Gautier, and P. Picart, "Evaluation of surface acoustic waves on the human skin using quasi-time-averaged digital Fresnel holograms," Appl. Opt. **52**, A136–A146 (2013).

[8] N. Verrier, D. Alexandre, and M. Gross, "Laser Doppler holographic microscopy in transmission: application to fish embryo imaging," Opt. Express **22**, 9368–9379 (2014).

[9] E. Leith and J. Upatnieks, "Reconstructed wavefronts and communication theory," J. Opt. Soc. Am. **52**, 1123–1128 (1962).

[10] R. Menzel and F. M. Shofner, "An investigation of Fraunhofer holography for velocimetry applications," Appl. Opt. **9**, 2073–2079 (1970).

[11] B. J. Thompson, J. H. Ward, and W. R. Zinky, "Application of hologram techniques for particle size analysis," Appl. Opt. **6**, 519–526 (1967).

[12] L. Onural and M. T. Özgen, "Extraction of three-dimensional object-location information directly

from in-line holograms using Wigner analysis," J. Opt. Soc. Am. A **9**, 252–260 (1992).

[13] L. Onural and P. D. Scott, "Digital decoding of in-line holograms," Opt. Eng. **26**, 1124–1132 (1987).

[14] S.H. Lee, Y. Roichman, G.R. Yi, S.H. Kim, S.M. Yang, A. van Blaaderen, P. van Oostrum, and D.G. Grier, "Characterizing and tracking single colloidal particles with video holographic microscopy," Opt. Express **15**, 18275–18282 (2007).

[15] S. Sotthivirat and J.A. Fessler, "Penalized likelihood image reconstruction for digital holography," J. Opt. Soc. Am. A **21**, 737–750 (2004).

[16] F. Soulez, L. Denis, C. Fournier, E. Thiébaut, and C. Goepfert, "Inverse-problem approach for particle digital holography: accurate location based on local optimization," J. Opt. Soc. Am. A **24**, 1164–1171 (2007).

[17] F. Soulez, L. Denis, E. Thiébaut, C. Fournier, and C. Goepfert, "Inverse problem approach in particle digital holography: out-of-field particle detection made possible," J. Opt. Soc. Am. A **24**, 3708–3716 (2007).

[18] C. Fournier, L. Denis, M. Seifi, and T. Fournel, "Digital Hologram Processing in On-Axis Holography," *Multi-dimensional Imaging.*, 51–74, John Wiley and Sons, (2014).

[19] D. J. Brady, K. Choi, D. L. Marks, R. Horisaki, and S. Lim, "Compressive holography," Opt. Express **17**, 13040–13049 (2009).

[20] S. Lim, D. L. Marks, and D. J. Brady, "Sampling and processing for compressive holography," Appl. Opt. **50**, H75–H86 (2011).

[21] Y. Rivenson, A. Stern, and B. Javidi, "Compressive Fresnel holography," J. Display Technol. **6**, 506–509 (2010).

[22] M. M. Marim, M. Atlan, E. Angelini, and J.-C. Olivo-Marin, "Compressed sensing with off-axis frequency-shifting holography," Opt. Lett. **35**, 871–873 (2010).

[23] G. Tyler and B. Thompson, "Fraunhofer holography applied to particle size analysis a reassessment," J. Mod. Opt. **23**, 685–700 (1976).

[24] C. S. Vikram, *Particle field holography*, vol. 11 (Cambridge University Press, 2005).

[25] S. D. Nicola, P. Ferraro, A. Finizio, and G. Pierattini, "Correct-image reconstruction in the presence of severe anamorphism by means of digital holography," Opt. Lett. **26**, 974–976 (2001).

[26] S. Grilli, P. Ferraro, S. D. Nicola, A. Finizio, G. Pierattini, and R. Meucci, "Whole optical wavefields reconstruction by digital holography," Opt. Express **9**, 294–302 (2001).

[27] S. D. Nicola, P. Ferraro, A. Finizio, and G. Pierattini, "Wave front reconstruction of Fresnel off-axis holograms with compensation of aberrations by means of phase-shifting digital holography," Opt. Lasers Eng. **37**, 331–340 (2002).

[28] J. S. Crane, P. Dunn, B. J. Thompson, J. Z. Knapp, and J. Zeiss, "Far-field holography of ampule contaminants," Appl. Opt. **21**, 2548–2553 (1982).

[29] N. Verrier, S. Coëtmellec, M. Brunel, and D. Lebrun, "Digital in-line holography in thick optical systems: application to visualization in pipes," Appl. Opt. **47**, 4147–4157 (2008).

[30] N. Verrier, C. Remacha, M. Brunel, D. Lebrun, and S. Coëtmellec, "Micropipe flow visualization using digital in-line holographic microscopy," Opt. Express **18**, 7807–7819 (2010).

[31] N. Verrier, S. Coëtmellec, M. Brunel, and D. Lebrun, "Determination of 3D-region of interest using digital in-line holography with astigmatic Gaussian beams," J. Europ. Opt. Soc. Rapid Pub. **4**, 09038 (2009).

[32] A. J. Lambert and D. Fraser, "Linear systems approach to simulation of optical diffraction," Appl. Opt. **37**, 7933–7939 (1998).

[33] H. T. Yura and S. G. Hanson, "Optical beam wave propagation through complex optical systems," J. Opt. Soc. Am. A **4**, 1931–1948 (1987).

[34] C. Palma and V. Bagini, "Extension of the Fresnel transform to abcd systems," J. Opt. Soc. Am. A **14**, 1774–1779 (1997).

[35] J. J. Wen and M. A. Breazeale, "A diffraction beam field expressed as the superposition of Gaussian beams," J. Acoust. Soc. Am. **83**, 1752–1756 (1988).

[36] L. Denis, D. A. Lorenz, and D. Trede, "Greedy solution of ill-posed problems: error bounds and exact inversion," Inverse Probl. **25**, 115017 (2009).

[37] L. Denis, D. Lorenz, E. Thiébaut, C. Fournier, and D. Trede, "Inline hologram reconstruction with sparsity constraints," Opt. Lett. **34**, 3475–3477 (2009).

[38] S. M. Kay, *Fundamentals of statistical signal processing: estimation theory.* (Prentice-Hall, 2010).

[39] C. Fournier, L. Denis, and T. Fournel, "On the single point resolution of on-axis digital holography," J. Opt. Soc. Am. A **27**, 1856–1862 (2010).

[40] P. Refregier, *Noise Theory and Application to Physics: From Fluctuations to Information.* (Springer Verlag, 2004).

[41] B. Lü and K. Duan, "Nonparaxial propagation of vectorial Gaussian beams diffracted at a circular aperture," Opt. Lett. **28**, 2440–2442 (2003).

[42] K. Duan and B. Lü, "Nonparaxial analysis of far-field properties of Gaussian beams diffracted at a circular aperture," Opt. Express **11**, 1474–1480 (2003).

[43] W. H. Press, T. A.Saul, W. T. Vetterling, and B. P. Flannery *Numerical Recipes in C, The Art of Scientific Computing.* (Cambridge University Press, 1992).